Research Square

Preprints are preliminary reports that have not undergone peer review.
They should not be considered conclusive, used to inform clinical practice,
or referenced by the media as validated information.

Polarization-resolved spectral tuning mechanism in frequency-selective hollow-core optical fibers

Muhammad Zain Siddiqui
Bilkent University
Ahmet E. Akosman
Roger Williams University
Mustafa Ordu
ordu@unam.bilkent.edu.tr

Bilkent University

Research Article

Keywords: Hollow-core fibers, Anti-resonant fibers, Negative curvature fibers, Spectral filtering, Selective transmission, Polarization

Posted Date: May 30th, 2026

DOI: https://doi.org/10.21203/rs.3.rs-9789328/v1

License: This work is licensed under a Creative Commons Attribution 4.0 International License.
Read Full License

Additional Declarations: No competing interests reported.

Abstract

Negative-curvature hollow-core fibers (NCFs) offer strong potential not only for ultra-low loss transmission but also for spectral filtering. However, precise control over frequency selectivity remains challenging in NCFs. Here, a unique design strategy for controlling wavelength-selective transmission in NCFs is demonstrated. A silica-based six-tube NCF with pole-supported concentric nested elements induces pole-mediated mode coupling and decoupling, resulting in filtering and transmitting of specific frequency bands in the near-IR spectrum, respectively. This spectral filtering response is extended to orthogonal polarizations by introducing transverse asymmetry through the form of nested tubes. The filtering bands for both polarization modes exhibit an approximately linear dependence on structural asymmetry, enabling independent tuning of polarization-resolved filtering bands at targeted wavelengths. An overall tuning span of *1.402 μm to 1.652 μm* is achieved within the telecommunication window, and a filtering band centered at *1.500 μm* is independently red-shifted to *1.550 μm* for both vertical- and horizontal-polarization modes. These results demonstrate promising spectral filtering control in NCFs and have great potential for applications including sensing, lasers, and spectroscopy.

1. Introduction

Conventional solid-core silica optical fibers form the backbone of worldwide communication and numerous practical applications; however, they are constrained by optical nonlinearity, chromatic dispersion, higher latency, and limited damage threshold, which impose fundamental limits and make further performance scaling challenging. Consequently, these limitations motivated the development of a new class of waveguides, hollow-core fibers (HCFs). Unlike conventional optical fibers, these novel HCFs confine and localize electromagnetic radiation within their hollow cores. The idea of guiding and transmitting light in air has intrigued the scientific community since the inception of optical fiber technology(Marcatili and Schmeltzer 1964). The hollow core in HCFs is typically air-filled, but it may also be filled with gases, liquids, or vacuumed, depending upon the desired optical properties(Cox et al. 2006; Debord et al. 2019; Mears et al. 2025; Pryamikov et al. 2024). The full potential of HCFs is reflected in their wide range of applications across optics, including medicine(Lombardini et al. 2018), security(Siddiqui et al. 2026), telecommunications(Gao et al. 2025; Petrovich et al. 2025), industrial processing(Shi et al. 2025), biology(Ermatov et al. 2020), and instrumentation(Digonnet and Chamoun 2016). One of the most important types of HCFs is the negative curvature hollow-core fiber (NCF), which employs hypocycloid or negatively curved cladding elements around an air core(Wei et al. 2017). Light guiding in NCFs is attributed to a combination of antiresonant reflection from the thin glass membranes and inhibited-coupling, in which coupling between core and cladding modes is reduced by small spatial mode overlap and a mismatch in their effective indices or wavenumbers(Melli et al. 2026; Poletti 2014; Wei et al. 2017). Owing to these guidance mechanisms, NCFs have recently been demonstrated with record-low attenuation below *0.1 dB/km*, highlighting their potential for next-generation low-loss transmission systems(Gao et al. 2025; Petrovich et al. 2025). In addition to ultra-low losses, NCFs offer low nonlinearity, reduced latency, strong higher-order mode suppression, and high damage thresholds(Fokoua et al. 2023; Ordu and Akosman 2022; Poletti 2014; Wei et al. 2017). Further, NCFs can

transmit at wavelengths where the solid silica core is opaque(Gao et al. 2018) or exhibits high bulk losses, such as in the mid-IR range(Knight and Yu 2013) or THz regime(Siddiqui et al. 2026), and they can provide longer light – matter interaction lengths in both linear and nonlinear regimes(Cassataro et al. 2017; Debord et al. 2019).

Engineered structural modifications in NCFs can enable a range of useful optical functionalities. Among these, polarization-maintenance and spectral-filtering phenomena can be achieved by appropriately designing the cladding geometry. In polarization-maintaining (PM) NCFs, the core symmetry is intentionally broken by introducing radial asymmetry, bi-thickness tubes, or a combination of both(Ding and Wang 2015; Hong et al. 2022; Hosen et al. 2022; Mousavi et al. 2016; Wei et al. 2023; Yerolatsitis et al. 2020; Zhu et al. 2022), thus creating an effective refractive index difference along the two principal axes and giving rise to two orthogonal polarization states. While the PM properties of NCFs have been investigated extensively over the last decade, spectral filtering in NCFs remains comparatively underexplored(Gamble et al. 2024; Siddiqui et al. 2024). Although discrete wavelengths are filtered through localized resonance/antiresonance conditions, which produce alternate high and low loss bands in NCFs, precise control over filtering at targeted wavelengths has not yet been achieved(Gamble et al. 2024; Siddiqui et al. 2024). For applications, such as lasers and spectroscopy, robust spectral filtering in HCFs is highly desirable(Couny and Benabid 2009). Apart from NCF designs, spectral filtering in optical fibers can be achieved via various methods, including fiber Bragg gratings (FBGs)(Wang et al. 2021), high-index regions surrounding the core(Aleshkina et al. 2021), refractive-index engineering in solid-core photonic crystal fibers (PCFs)(Sun 2007), or plasmonic effects in metal-coated cladding components(Dou et al. 2016).

In this study, we propose unique NCF designs to precisely control the spectral filtering. The six-tube silica-based NCF geometry employs concentric nested tubes that are mechanically supported by radial pole anchors. These anchors cause a fluctuating loss profile consisting of high- and low-loss bands at discrete wavelengths. In the high-loss bands, light couples to the poles and leaks out, resulting in rejected wavelengths. In contrast, weaker coupling in the low-loss bands produces transmitted (filtered) wavelengths. Subsequently, polarization splitting of the core modes is achieved by introducing ellipticity in the nested tubes along a chosen polarization direction. Increasing the ellipticity of nested tubes along one of the polarization directions causes an approximately linear spectral shift of the filtered bands corresponding to that polarization mode, enabling the control of the filtered wavelength shift as a function of ellipticity. Consequently, a filtering band centered at *1.500 μm* is red-shifted by *50 nm* to *1.550 μm* by adjusting the ellipticity. The same approach is extended to the orthogonal polarization mode by tuning the ellipticity of the nested tubes along the corresponding polarization axis, yielding a similar spectral shift. Thus, independent spectral filtering control is achieved for both polarizations.

2. Fiber design and simulation procedure

The schematic cross-sectional views of the proposed NCFs are shown in Fig. 1. The silica-based fiber geometries consist of a six-tube structure with concentric nested tubes. Two fiber design approaches

are considered, one of which comprises suspended nested tubes without any anchor or support, including the suspended tubular NCF (ST-NCF), suspended elliptic-tubular NCF (SET-NCF), and suspended elliptic NCF (SE-NCF), as depicted in Fig. 1(a-c), respectively. ST-NCF includes suspended circular nested tubes with design parameters, core diameter, *D*, cladding tube diameter, d_1, nested cladding tube diameter, d_2, and strut thickness, *t*. In the SET-NCF design, two elliptical nested tubes are introduced in the horizontal direction with an ellipticity ratio $r_x = d_3/d_2$, whereas round nested tubes are retained in the vertical direction. Moreover, in the SE-NCF structure, all the suspended nested tubes are elliptical, where the ellipticity for the nested tubes in the vertical direction is defined by $r_y = d_4/d_2$, while the ellipticity (r_x) for elliptical tubes in the horizontal direction is held constant. These fibers include suspended elements that are impractical. However, fabrication-feasible fibers can be realized by incorporating radial pole anchors to support the suspended cladding elements. Pole-supported tubular NCF (PT-NCF), pole-supported elliptic-tubular NCF (PET-NCF), and pole-supported elliptic NCF (PE-NCF) are the pole-anchored counterparts of ST-NCF, SET-NCF, and SE-NCF, respectively, as shown in Fig. 1(d-f). The diameter difference between d_1 and d_2 defines the pole-anchor length.

SET-NCF and SE-NCF incorporate dissimilar cladding elements along orthogonal directions relative to ST-NCF, breaking the fiber core symmetry, as observed in Fig. 1(a-c). Such a core asymmetry is a defining feature of polarization-maintaining (PM) fibers, in which the effective refractive index differs along the two principal axes. Consequently, the guided modes become birefringent, which leads to polarization-dependent confinement losses and a clear splitting between the horizontal polarization (H-pol) and vertical polarization (V-pol) fundamental modes. The same observation holds for the pole-anchored counterparts.

The proposed fiber designs are numerically investigated using a finite-element method (FEM) based electromagnetic wave frequency-domain (EWFD) solver in COMSOL Multiphysics. To study the guidance properties of the fibers through FEM-based modal analysis, careful meshing of the studied structures is necessary. Therefore, convergence studies were conducted, following the methodology described in(Akcımen et al. 2026), to optimize the modeling parameters for improved transmission performance. A minimum of *5* meshes were added to the narrow regions of the cladding with a maximum mesh size of *~ λ/6*. A circular perfectly matched layer (PML) with an optimum thickness of *10 μm* is also employed around the fiber to minimize the back reflections. Before the formal numerical study, a baseline geometry optimization was performed at *1.550 μm* to define common design parameters for all fiber designs. The baseline-optimized parameters are fixed throughout the analysis at *D = 30 μm*, *t = 0.46 μm*, d_1 *= 25 μm*, and d_2 *= 12.5 μm*.

3. Impact of structural perturbations on confinement in NCFs

The placement and geometry of the nested cladding elements in NCFs strongly influence modal confinement and leakage loss, as summarized in Fig. 2, which presents cross-sectional fiber geometries, confinement loss spectra over *1–1.8 μm*, and representative electric-field mode profiles at selected

wavelengths. Initially, different nested tube spatial positions are compared to find the configuration with the lowest confinement loss. For benchmarking, a nested tubular NCF (NT-NCF) is designed using the same baseline parameters as the ST-NCF. In the NT-NCF, the nested tube is laterally offset from the center and fused to the outer cladding tube. In contrast, ST-NCF employs concentric nested tubes without any support, as illustrated in the schematic cross-section in Fig. 2(a). The confinement loss spectra in Fig. 2(a) indicate that the concentric nested tube layout in ST-NCF reduces the leakage loss by approximately two orders of magnitude relative to NT-NCF. The electric-field mode profiles at $\lambda = 1.500\ \mu m$ for ST-NCF and NT-NCF are shown in Fig. 2(a), indicating tight confinement in ST-NCF, whereas NT-NCF exhibits increased leakage near the contact region where the nested tube is connected to the outer cladding tube. Overall, these results confirm that the concentric nested tube configuration in ST-NCF provides superior confinement and significantly lower leakage loss than the NT-NCF.

Next, we investigate how modifying the nested tube geometry affects the confinement. Transforming the ST-NCF structure into SET-NCF by replacing the circular nested tubes in the horizontal direction with the elliptical nested tubes having an ellipticity ratio r_x, while the vertical nested tubes remain circular, and all other parameters are kept constant, as shown in Fig. 2(b). This controlled perturbation breaks the core symmetry, enabling the quantification of polarization-resolved confinement-loss spectra. A parametric sweep of r_x at the center wavelength of $1.550\ \mu m$ indicated that increasing the ellipticity ratio

enhanced the confinement loss splitting between the fundamental polarization modes. This occurs because the H-pol experiences higher losses with an increase in r_x, while the V-pol loss remains essentially constant. Therefore, a parametric wavelength sweep was conducted at $r_x = 1.7$, for which the confinement loss spectrum for SET-NCF is shown in Fig. 2(b). The V-pol response of SET-NCF closely matches that of ST-NCF, whereas the H-pol spectrum is shifted toward higher loss values, indicating increased leakage for the H-pol. This difference arises from the anisotropic nature of the cladding elements. The V-pol mode is effectively confined by four cladding elements in the vertical direction, whereas the H-pol mode is confined by only two cladding elements in the horizontal direction, resulting in weaker confinement and higher leakage loss as evident in the mode profiles of H-pol and V-pol at $\lambda = 1.500\ \mu m$ shown in Fig. 2(b).

ST-NCF and SET-NCF are ideal designs but are not feasible for practical consideration in their suspended nested-tube form. Therefore, we introduced radial pole anchors in these designs to mechanically support nested tubes while preserving their intended geometry and keeping all design parameters unchanged. The resulting PT-NCF, the pole-anchored counterpart of ST-NCF, exhibits a periodic, fluctuating confinement-loss profile with alternating high- and low-loss regions, as shown in Fig. 2(c). These extrema arise from local resonance and anti-resonance conditions and correspond to wavelength-selective transmission at discrete wavelengths. In this context, high-loss regions are associated with unfiltered (rejected) wavelengths, whereas low-loss regions are attributed to filtered (transmitted) wavelength windows. This wavelength-selective behavior in PT-NCF originates from the pole anchors, which introduce additional coupling pathways. In the unfiltered spectral regions, the guided field couples strongly to the pole anchors, enhancing leakage and producing high-loss bands. Conversely, the modal

field remains largely decoupled from the pole anchors in the filtered regions, resulting in low-loss transmission windows. The electric field mode profiles shown in Fig. 2(c) highlight strong field coupling to the pole anchors at $\lambda = 1.456\ \mu m$ and $1.512\ \mu m$, where the mode clearly leaks into and radiates along the pole anchors, corresponding to rejected (unfiltered) bands. In contrast, at $\lambda = 1.500\ \mu m$, such pole anchor coupling is largely absent, and the field remains well confined within the core. Notably, the filtering bands near $\sim 1.600\ \mu m$ exhibit paired peaks as shown in the confinement spectrum in Fig. 2(c).

Similarly, PET-NCF, the pole-anchored counterpart of SET-NCF, exhibits spectral filtering induced by pole anchors as shown in Fig. 2(d). Unlike PT-NCF, the confinement-loss spectrum for PET-NCF is polarization-resolved because the cladding contains elliptic tubes ($r_x = 1.7$) along the horizontal axis, leading to distinct filtering bands for H-pol and V-pol. Consequently, the filtering bands for H-pol and V-pol occur predominantly at different spectral locations, indicating polarization-specific shifts in the filtered wavelengths. Those spectral shifts in the filtering bands are observed primarily for H-pol due to the presence of elliptical nested tubes along the horizontal direction. However, the V-pol filtering bands remain at the same spectral locations as in PT-NCF because circular nested tubes are retained along the vertical axis. The mode profiles (in Fig. 2(d)) also capture the H-pol spectral shift, with representative fields shown at $\lambda = 1.456\ \mu m, 1.490\ \mu m$, and $1.500\ \mu m$. Notably, the filtered (low-loss) wavelength is $1.500\ \mu m$ for V-pol, whereas it shifts to $1.490\ \mu m$ for H-pol, consistent with the polarization-resolved shift of the filtering bands. Also, the electric field profiles for the V-pol at $\lambda = 1.456\ \mu m, 1.500\ \mu m$, and $1.512\ \mu m$ confirm that the V-pol filtering bands in PET-NCF remain at the same spectral positions as in PT-NCF, while indicating that V-pol in PET-NCF exhibits higher confinement loss than PT-NCF. In particular, the mode profile at $\lambda = 1.500\ \mu m$ shows higher leakage loss in PET-NCF than in PT-NCF.

To facilitate a focused interpretation of the physical origin of the H-pol spectral shift in PET-NCF, the analysis will be limited to the telecommunications window spanning $1.250–1.675\ \mu m$. Within this band, we systematically evaluate how anisotropic cladding geometry with pole anchors governs the polarization-resolved displacement of the filtering bands.

4. Impact of ellipticity ‘rx’ on spectral selectivity in PET-NCF

In PET-NCF, the filtered wavelengths in H-pol are spectrally displaced compared to the largely fixed filtered band positions in V-pol, as discussed in the previous section. These shifts in H-pol are associated with the elliptical nested tubes along the horizontal axis in the PET-NCF structure, which modify the coupling behavior with the pole anchors for H-pol. Understanding the physical basis of this wavelength displacement is essential for engineering the filtered bands at target wavelengths. The cross-sectional schematic of PET-NCF is shown in Fig. 3(a), together with an enlarged view of the elliptical nested tube defining r_x in the horizontal direction, where the ellipse minor axis is fixed at $d_2 = 12.5\ \mu m$. Figures 3 (b-f) demonstrates the evolution of the spectral filtering response of PET-NCF as r_x is increased from 0.6 to 1.7. At $r_x = 0.6$, no wavelength selectivity is observed for either H-pol or V-pol, since strong modal coupling to the pole anchors produces high leakage loss as shown in Fig. 3(b). When the r_x is increased

to *0.8* in Fig. 3(c), V-pol begins to exhibit well-defined, stable filtering bands, while H-pol still does not show a clear filtering response because the mode continues to couple strongly to the pole anchors. For $r_x > 1$, H-pol begins to develop distinct filtering bands, which become increasingly separated from the V-pol bands as r_x increases from *1.1* to *1.7*. In contrast, the V-pol filtered wavelengths remain at the same spectral locations and retain a similar confinement-loss profile across this range of r_x. Moreover, Figs. 3(c-f) indicates that the number of V-pol filtered wavelengths remains constant at *8* for $r_x = 0.8–1.7$. In contrast, the H-pol filtered-wavelength count increases with ellipticity, reaching *8, 10*, and *11* at $r_x = 1.1$, *1.4*, and *1.7*, respectively (Figs. 3(d-f)). Thus, the shift of the H-pol filtering bands relative to V-pol is not primarily caused by a continuous displacement of the existing H-pol filtered wavelengths with increasing ellipticity, but rather dominated by the emergence of additional H-pol filtering bands as r_x increases. Among these cases, the most notable result is obtained at $r_x = 1.7$, which provides the strongest polarization splitting and the largest spectral separation between the H-pol and V-pol filtered bands as illustrated in Fig. 3(f). Figure 4(a) further shows that the V-pol filtered-band positions in PET-NCF at $r_x = 1.7$ align with those of PT-NCF, since both structures employ circular nested tubes. The V-pol confinement loss in PET-NCF, however, fluctuates to higher loss values across the spectrum due to the elliptic nested tubes.

Now that the physical origin of the H-pol filtered-wavelength shift is explored, r_x can be fine-tuned to position a selected H-pol filtering band at a desired target wavelength. Figure 4(b) shows the shift of the *1.500 μm* H-pol filtered band as a function of r_x. At the zero-shift condition ($r_x = 1.0$), one of the filtering bands is centered at *1.500 μm*, indicating PT-NCF behavior. As the r_x is increased, this filtered band exhibits spectral displacement that can be tuned. Over the explored range, the displacement is approximately linear, with a maximum red shift of *+ 152 nm* (placing the band at *1.652 μm*) and a maximum blue shift of *-98 nm* (placing the band at *1.402 μm*). For instance, shifting the *1.500 μm* filtered band to *1.550 μm* requires a *+ 50 nm* shift, which can be achieved at $r_x = 1.13$ as shown in Fig. 4(b). The corresponding H-pol confinement-loss spectra for PET-NCF at $r_x = 1.0$ and *1.13* are compared in Fig. 4(c), confirming a shift in filtered wavelength from *1.500 μm* to *1.550 μm*.

Similarly, the V-pol filtering bands in PE-NCF may be tuned by adjusting the ellipticity 'r_y' of nested ellipses in the vertical axis while keeping the ellipticity 'r_x' of nested ellipses in the horizontal axis fixed (e.g., $r_x = 1.7$), enabling independent placement of the V-pol filtered bands at desired target wavelengths.

5. Impact of ellipticity 'ry' on spectral selectivity in PE-NCF

Since V-pol confinement is mainly affected by the cladding geometry along the vertical axis, changing the ellipticity 'r_y' of the nested ellipse in the vertical direction provides an effective way to control the V-pol spectral filtering response in PE-NCF. Figure 5(a) depicts SE-NCF, with an inset zooming in a nested ellipse in the vertical direction by defining r_y at a fixed $d_2 = 12.5\ \mu m$. The investigation started with the SE-NCF structure to examine how polarization behavior varies with r_y while keeping r_x constant at *1.7*.

Figure 5(b) shows the loss spectrum of SE-NCF at $\lambda = 1.550\ \mu m$ as a function of r_y, with $r_x = 1.7$ held constant. As a result, the H-pol confinement loss spectrum remains unchanged, while the V-pol loss varies systematically with r_y over the range *0.6–1.8*. Both H-pol and V-pol exhibit elevated confinement loss for $r_y < 0.6$. As r_y increases beyond *0.6*, the V-pol leakage loss decreases to a minimum at the optimum value of $r_y = 0.8$, yielding a maximum loss separation between H-pol and V-pol modes. Further increasing r_y leads to a rise in the V-pol confinement loss, which eventually converges to the H-pol mode loss at $r_y = 1.7$. At this point, the polarization-dependent loss splitting vanishes, and the SE-NCF structure no longer exhibits PM behavior.

Figure 5(c) shows the PE-NCF structure, a pole-anchored counterpart of SE-NCF, with fixed $r_x = 1.7$, while Figs. 5(d–h) display the evolution of PE-NCF confinement-loss spectra as r_y varies. The confinement loss spectra of PE-NCF feature clear wavelength-filtering bands for both H-pol and V-pol due to the pole supports, as shown in Figs. 5(d-g). Since r_x is constant, the H-pol filtering bands do not shift in frequency, and their positions remain fixed as r_y changes. However, the H-pol filtering bands gradually increase in loss levels with larger r_y as observed in Figs. 5(d-g). Meanwhile, the V-pol filtering bands show an apparent spectral shift as r_y increases. This shift in V-pol is not primarily a smooth translation of existing bands but rather results from the appearance of new filtering bands as r_y rises. The H-pol filtered-wavelength count remains constant at *11*, whereas the V-pol count increases from *7* to *8*, *10*, and *11* at r_y = *0.95*, *1.10*, *1.40*, and *1.60*, respectively. When $r_y = 1.70$, the PE-NCF loses polarization splitting and behaves as a non-PM fiber, with identical H-pol and V-pol filtering responses and a filtered-wavelength count of *11*, as shown in Fig. 5(h).

It is evident in Fig. 6(a) that the H-pol filtering band positions in PE-NCF ($r_y = 1.6$ & $r_x = 1.7$) remain largely aligned with H-pol filtering bands of PET-NCF ($r_y = 1.0$ & $r_x = 1.7$). However, the H-pol filtering bands in PE-NCF exhibit higher loss levels than in PET-NCF, which is attributed to the presence of elliptical nested tubes along the vertical axis. As r_y increases, the V-pol filtering response in PE-NCF shifts, allowing V-pol filtering bands to be positioned at prescribed target wavelengths as shown in Fig. 6(b) and Fig. 6(c). Figure 6(b) illustrates the spectral shift of the V-pol filtering band initially positioned at *1.500 μm*, where the zero-shift condition corresponds to the PET-NCF behavior at $r_y = 1.0$ and $r_x = 1.7$. As r_y increases, the V-pol filtering band in PE-NCF exhibits two tuning directions in Fig. 6(b): a red shift toward longer wavelengths and a blue shift toward shorter wavelengths, analogous to the H-pol filtering band tuning observed for PET-NCF in Fig. 4(b). The filtered wavelength spectral displacements in PET-NCF are approximately linear, with the filtering band at *1.652 μm* and *1.402 μm*, corresponding to maximum red shifts of *+ 152 nm* and maximum blue shifts of *-98 nm* at $r_y = 1.4$ and *1.8*, respectively. Similar shifting behavior is observed for the *1.500 μm* filtering band in V-pol of PE-NCF and H-pol of PET-NCF, with nearly identical maximum red and blue shifts occurring at the same corresponding ellipticity values (Fig. 4(b) and Fig. 6(b)). The *1.500 μm* V-pol filtering band in PE-NCF can be shifted to *1.550 μm* by increasing r_y to *1.125* while keeping $r_x = 1.7$ constant, which corresponds to the red shift of *+ 50 nm* as indicated in

Fig. 6(b). The resulting V-pol confinement-loss spectra for PE-NCF at $r_y = 1.0$ and $r_y = 1.125$ are shown in Fig. 6(c), demonstrating a shift in the filtered wavelength from *1.500 μm* to *1.550 μm*.

6. Polarization-resolved filtered wavelength counts

The analyses in Sections 4 and 5 show that the spectral shifts observed in PET-NCF and PE-NCF for filtered wavelengths with varying r_x and r_y arise primarily from the emergence of additional filtering bands, rather than from a continuous displacement of existing bands. Consequently, different combinations of r_x and r_y are expected to produce different filtered wavelength counts for H-pol (PET-NCF) and V-pol (PE-NCF). To quantify this behavior, a comprehensive parametric study of all combinations of r_x and r_y in the range *0.8–1.8*, evaluating the filtering response within the telecommunication bandwidth (*1.250–1.675 μm*) for both polarizations, is summarized in the contour maps in Fig. 7.

In Fig. 7(a) and Fig. 7(b), along the diagonal where the ellipticities of nested tubes in orthogonal directions are equal (i.e., $r_x = r_y$), the fiber geometries approach transverse symmetry. As a result, polarization splitting vanishes, and the fibers behave as non-PM fibers, with both polarizations exhibiting the same filtered wavelength counts along the diagonal. Away from the diagonal, the H-pol filtered wavelength counts in Fig. 7(a) show a comparatively irregular dependence on r_x and r_y. However, for ellipticity combinations below the diagonal, a clearer pattern emerges where, at fixed r_y, the H-pol filtered wavelength count increases with r_x, reaching a maximum count of *11* around $r_x = 1.6–1.7$. In contrast, the V-pol filtered wavelength count exhibits a more systematic increase with r_y at fixed r_x, attaining a maximum count of *11* near $r_y = 1.6–1.7$.

At larger ellipticities (for both r_x and r_y *as 1.8*) in Fig. 7(a) and Fig. 7(b), the filtered wavelength counts decrease for both polarizations, which is attributed to a reduced air gap between the nested ellipses and outer circular cladding tubes, which strengthens the coupling/leakage pathways and degrades the filtering ability. Overall, the contour maps indicate a smoother and more robust filtering response for V-pol under r_y tuning than for H-pol under r_x tuning. This behavior is consistent with stronger vertical confinement provided by four cladding elements for V-pol along the vertical direction, compared with only two for H-pol along the horizontal direction. These results suggest that improving H-pol filtering robustness to the level of V-pol may require increasing the effective horizontal cladding support via an eight-tube NCF structure, a promising direction for future work.

7. Conclusion

This work introduces and numerically investigates a family of frequency-selective NCFs that exploit fiber core anisotropy and polarization states to control spectral filtering. Starting with six tube-nested-element geometries, it was first established that the concentric nested element configuration (i.e., ST-NCF) substantially reduces confinement losses by approximately two orders of magnitude in the studied

spectrum compared to NT-NCF. By introducing ellipticities r_x and r_y into the concentric nested tube configurations (i.e., SET-NCF and SE-NCF) in the horizontal and vertical directions, respectively, the fibers demonstrated polarization-resolved confinement-loss spectra. Next, radial pole anchors were introduced into the suspended nested tube NCFs configuration to transition to fabrication-feasible geometries, yielding PT-NCF, PET-NCF, and PE-NCF variants. The pole supports a clear wavelength-selective response, characterized by alternating high- and low-loss regions, attributable to local resonance/antiresonance and anchor-mediated coupling. Importantly, the polarization-resolved "spectral shifts" observed in PET-NCF and PE-NCF with changing r_x and r_y, respectively, were shown to be governed predominantly by the emergence of additional filtering bands, rather than a continuous translation of existing bands. Based on a physical understanding of spectral filtering behavior, practical guidelines were developed for positioning the filtered band within the telecom window at the target wavelength for both polarization modes. The shift in H-pol and V-pol filtered band positions showed nearly linear dependence on r_x and r_y, respectively. Therefore, both r_x and r_y provided direct adjustment to independently tune the H-pol and V-pol bands, allowing the *1.500 μm* filtered band to red shift to *1.550 μm*, with a total tuning range approximately from *1.402* to *1.652 μm*. Further, contour-map analyses across r_x and r_y in the *1.250–1.675 μm* telecom band further quantified the filtered-wavelength range for each polarization, showing generally smoother, more stable filtering performance for V-pol under r_y control than for H-pol under r_x control. Overall, this study establishes, to the best of our knowledge, the first demonstration of independently tunable polarization-resolved spectral filtering in NCFs.

Declarations

The authors declare no conflicts of interest.

Funding.

This work received no external funding.

Author Contribution

M.Z.S. performed numerical studies, formal analysis, and visualization, and wrote the original manuscript; A.E.A. performed formal analysis and conceptual design; M.O. supervised the project, provided infrastructure, and performed formal analysis and conceptual design. All authors have contributed to the review and editing of the manuscript.

Data Availability

The data that support the findings of this study are available from the corresponding author.

References

1. Akcımen, S., Siddiqui, M.Z., Chiba, K., Kanamori, Y., Ordu, M.: Implementing elliptical cladding elements in terahertz negative curvature hollow-core waveguides. Opt. Mater. Express OME. **16**, 419–432 (2026). https://doi.org/10.1364/OME.582823
2. Aleshkina, S., Kashaykina, T., Yashkov, M., Salganskii, M., Velmiskin, V., Bubnov, M., Likhachev, M.: Spectral filtering in single-mode fibers using resonant coupling with absorbing rods. Opt. Lett. OL. **46**, 1458–1461 (2021). https://doi.org/10.1364/OL.412429
3. Cassataro, M., Novoa, D., Günendi, M.C., Edavalath, N.N., Frosz, M.H., Travers, J.C., Russell, P.S.J.: Generation of broadband mid-IR and UV light in gas-filled single-ring hollow-core PCF. Opt. Express OE. **25**, 7637–7644 (2017). https://doi.org/10.1364/OE.25.007637
4. Couny, F., Benabid, F.: Optical frequency comb generation in gas-filled hollow core photonic crystal fibres. J. Opt. A: Pure Appl. Opt. **11**, 103002 (2009). https://doi.org/10.1088/1464-4258/11/10/103002
5. Cox, F.M., Argyros, A., Large, M.C.J.: Liquid-filled hollow core microstructured polymer optical fiber. Opt. Express OE. **14**, 4135–4140 (2006). https://doi.org/10.1364/OE.14.004135
6. Debord, B., Amrani, F., Vincetti, L., Gérôme, F., Benabid, F.: Hollow-Core Fiber Technology: The Rising of Gas. Photonics Fibers. **7**, 16 (2019). https://doi.org/10.3390/fib7020016
7. Digonnet, M.J.F., Chamoun, J.N.: Recent developments in laser-driven and hollow-core fiber optic gyroscopes. In: Fiber Optic Sensors and Applications XIII. pp. 19–29. SPIE (2016)
8. Ding, W., Wang, Y.-Y.: Hybrid transmission bands and large birefringence in hollow-core anti-resonant fibers. Opt. Express OE. **23**, 21165–21174 (2015). https://doi.org/10.1364/OE.23.021165
9. Dou, C., Jing, X., Li, S., Liu, Q., Bian, J.: A Photonic Crystal Fiber Polarized Filter at 1.55 μm Based on Surface Plasmon Resonance. Plasmonics. **11**, 1163–1168 (2016). https://doi.org/10.1007/s11468-015-0155-4
10. Ermatov, T., Noskov, R.E., Machnev, A.A., Gnusov, I., Atkin, V., Lazareva, E.N., German, S.V., Kosolobov, S.S., Zatsepin, T.S., Sergeeva, O.V., Skibina, J.S., Ginzburg, P., Tuchin, V.V., Lagoudakis, P.G., Gorin, D.A.: Multispectral sensing of biological liquids with hollow-core microstructured optical fibres. Light Sci. Appl. **9**, 173 (2020). https://doi.org/10.1038/s41377-020-00410-8
11. Fokoua, E.N., Mousavi, S.A., Jasion, G.T., Richardson, D.J., Poletti, F.: Loss in hollow-core optical fibers: mechanisms, scaling rules, and limits. Adv. Opt. Photon AOP. **15**, 1–85 (2023). https://doi.org/10.1364/AOP.470592
12. Gamble, J., Ordu, M., Akosman, A.E.: Frequency selective low-loss transmission in negative curvature hollow-core fibers. Phys. Scr. **99**, 055535 (2024). https://doi.org/10.1088/1402-4896/ad3a48
13. Gao, S., Chen, H., Xiong, Y., Sun, Y., Ding, W., Wang, Y.: 40 Km, 0.052 Db/Km and 83 Km, 0.076 Db/Km in Interstitial-Tube-Assisted Hollow-Core Fibre. In: 2025 European Conference on Optical Communications (ECOC). pp. 1–4 (2025)

14. Gao, S.-F., Wang, Y.-Y., Ding, W., Wang, P.: Hollow-core negative-curvature fiber for UV guidance. Opt. Lett. OL. **43**, 1347–1350 (2018). https://doi.org/10.1364/OL.43.001347
15. Hong, Y., Gao, S., Ding, W., Zhang, X., Jia, A., Sheng, Y., Wang, P., Wang, Y.: Laser Photonics Rev. **16**, 2100365 (2022). https://doi.org/10.1002/lpor.202100365 Highly Birefringent Anti-Resonant Hollow-Core Fiber with a Bi-Thickness Fourfold Semi-Tube Structure
16. Hosen, M.S., Khaleque, A., Shaha, K.S.R., Asha, L.N., Sultana, A.S., Nishad, R., Rahman, M.T.: Highly birefringent polarization maintaining low-loss single-mode hollow-core antiresonant fiber. Opt. Continuum OPTCON. **1**, 2167–2184 (2022). https://doi.org/10.1364/OPTCON.464884
17. Knight, J.C., Yu, F.: Silica Hollow Core Fibers for Mid-IR Wavelengths. In: Workshop on Specialty Optical Fibers and their Applications (2013), paper T2.1. p. T2.1. Optica Publishing Group (2013)
18. Lombardini, A., Mytskaniuk, V., Sivankutty, S., Andresen, E.R., Chen, X., Wenger, J., Fabert, M., Joly, N., Louradour, F., Kudlinski, A., Rigneault, H.: High-resolution multimodal flexible coherent Raman endoscope. Light Sci. Appl. **7**, 10 (2018). https://doi.org/10.1038/s41377-018-0003-3
19. Marcatili, E.J., Schmeltzer, R.A.: Hollow Metallic and Dielectric Waveguides for Long Distance Optical Transmission and Lasers. Bell Syst. Tech. J. **43**, 1783–1809 (1964). https://doi.org/10.1002/j.1538-7305.1964.tb04108.x
20. Mears, R., Vorobiev, D., Harrington, K., Indahl, B., Stone, J.M., Fleming, B., Birks, T.A., Wadsworth, W.J.: Anti-resonant hollow core optical fibres for the vacuum-ultraviolet. In: Conference on Lasers and Electro-Optics/Europe (CLEO/Europe 2025) and European Quantum Electronics Conference (EQEC 2025) (2025), paper ce_2_3. p. ce_2_3. Optica Publishing Group (2025)
21. Melli, F., Rosa, L., Vasko, K., Benabid, F., Vincetti, L.: Disentangling Loss Mechanisms to Bridge Inhibited-Coupling and Anti-Resonant Models in Hollow-Core Fibers. J. Lightwave Technol. 1–11 (2026). https://doi.org/10.1109/JLT.2026.3674574
22. Mousavi, S.A., Sandoghchi, S.R., Richardson, D.J., Poletti, F.: Broadband high birefringence and polarizing hollow core antiresonant fibers. Opt. Express OE. **24**, 22943–22958 (2016). https://doi.org/10.1364/OE.24.022943
23. Ordu, M., Akosman, A.E.: Re-thinking the design of low-loss hollow-core fibers via optimal positioning of the nested elements. Opt. Lett. OL. **47**, 3039–3042 (2022). https://doi.org/10.1364/OL.455118
24. Petrovich, M., Numkam Fokoua, E., Chen, Y., Sakr, H., Adamu, A.I., Hassan, R., Wu, D., Fatobene Ando, R., Papadimopoulos, A., Sandoghchi, S.R., Jasion, G., Poletti, F.: Broadband optical fibre with an attenuation lower than 0.1 decibel per kilometre. Nat. Photon. **19**, 1203–1208 (2025). https://doi.org/10.1038/s41566-025-01747-5
25. Poletti, F.: Nested antiresonant nodeless hollow core fiber. Opt. Express OE. **22**, 23807–23828 (2014). https://doi.org/10.1364/OE.22.023807
26. Pryamikov, A.D., Gladyshev, A.V., Kosolapov, A.F., Bufetov, I.A.: Hollow-core optical fibers: current state and development prospects. Phys. Usp. **67**, 129–156 (2024)

27. Shi, J., Rao, B., Chen, Z., Wang, Z., Sun, G., Xu, Z., Huang, Z., Li, P., Dong, Z., Fu, M., Tian, X., Yang, B., Zhang, J., Zhou, Z., Li, T., Zhang, L., Shui, B., Gao, C., Chen, J.: All-fiber highly efficient delivery of 2 kW laser over 2.45 km hollow-core fiber. Nat. Commun. **16**, 8965 (2025). https://doi.org/10.1038/s41467-025-64073-y
28. Siddiqui, M.Z., Akosman, A.E., Ordu, M.: Enhancing polarization maintenance and spectral filtering in negative curvature hollow-core fibers. Photonics Nanostruct. Fundam. Appl. **58**, 101221 (2024). https://doi.org/10.1016/j.photonics.2023.101221
29. Siddiqui, M.Z., Chiba, K., Kanamori, Y., Ordu, M.: Terahertz waveguiding through 3D-Printed Bar-Nested Hollow-Core optical fibers. Opt. Fiber. Technol. **98**, 104529 (2026). https://doi.org/10.1016/j.yofte.2025.104529
30. Sun, X.: Wavelength-selective coupling of dual-core photonic crystal fiber with a hybrid light-guiding mechanism. Opt. Lett. OL. **32**, 2484–2486 (2007). https://doi.org/10.1364/OL.32.002484
31. Wang, Y., Tao, J., Yuan, W., Lian, Z., Ling, Q., Chen, D., Yu, Z., Lu, C.: Hollow Core Bragg Fiber Integrated With Regenerate Fiber Bragg Grating for Simultaneous High Temperature and gas Pressure Sensing. J. Lightwave Technol. **39**, 5643–5649 (2021). https://doi.org/10.1109/JLT.2021.3088530
32. Wei, C., Weiblen, R.J., Menyuk, C.R., Hu, J.: Negative curvature fibers. Adv. Opt. Photon AOP. **9**, 504–561 (2017). https://doi.org/10.1364/AOP.9.000504
33. Wei, S., Zhang, Y., Wu, T., Hou, Z., Xia, C., Liu, J., Zhou, G.: Broadband birefringence hollow-core anti-resonant optical fiber with elliptical air holes. Opt. Commun. **527**, 128976 (2023). https://doi.org/10.1016/j.optcom.2022.128976
34. Yerolatsitis, S., Shurvinton, R., Song, P., Zhang, Y., Francis-Jones, R.J.A., Rusimova, K.R.: Birefringent Anti-Resonant Hollow-Core Fiber. J. Lightwave Technol. **38**, 5157–5162 (2020). https://doi.org/10.1109/JLT.2020.3000706
35. Zhu, Y., Li, W., Gao, F., Xu, X., Song, N.: Small-core hollow-core nested antiresonant nodeless fiber with semi-circular tubes. Opt. Express OE. **30**, 20373–20388 (2022). https://doi.org/10.1364/OE.460185

Figures

Fig 1: Fiber Designs

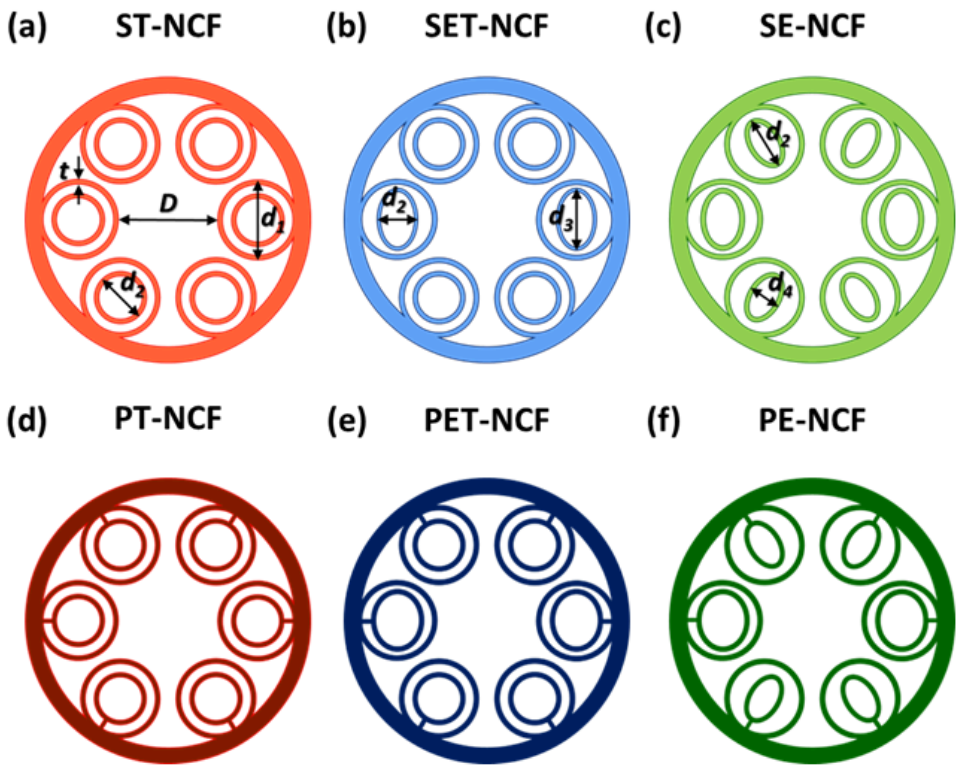


Figure 1

Schematic cross sections of the proposed NCFs with concentric nested elements: (a) suspended tubular NCF (ST-NCF) with round nested cladding elements, (b) suspended elliptic-tubular NCF (SET-NCF) in which nested cladding elements are round and elliptic in the vertical and horizontal directions, respectively, and (c) suspended elliptic NCF (SE-NCF) with all nested elements as elliptical tubes. (d) Pole-supported tubular NCF (PT-NCF), (e) pole-supported elliptic-tubular NCF (PET-NCF), and (f) pole-

supported elliptic NCF (PE-NCF) are the corresponding fiber designs of ST-NCF, SET-NCF, and SE-NCF, respectively, with nested cladding elements anchored with poles. The primary design parameters are depicted in (a), showing the core diameter, *D*, strut thickness, *t*, outer cladding tubes' diameter, d_1, and nested cladding tubes' diameter, d_2, whereas the design parameters d_2 and d_3 in (b) and d_2 and d_4 *in* (c) depict the minor and major axes for nested elliptic tubes, respectively. All fibers feature the same *D*, d_1, d_2, and *t* for better performance comparison.

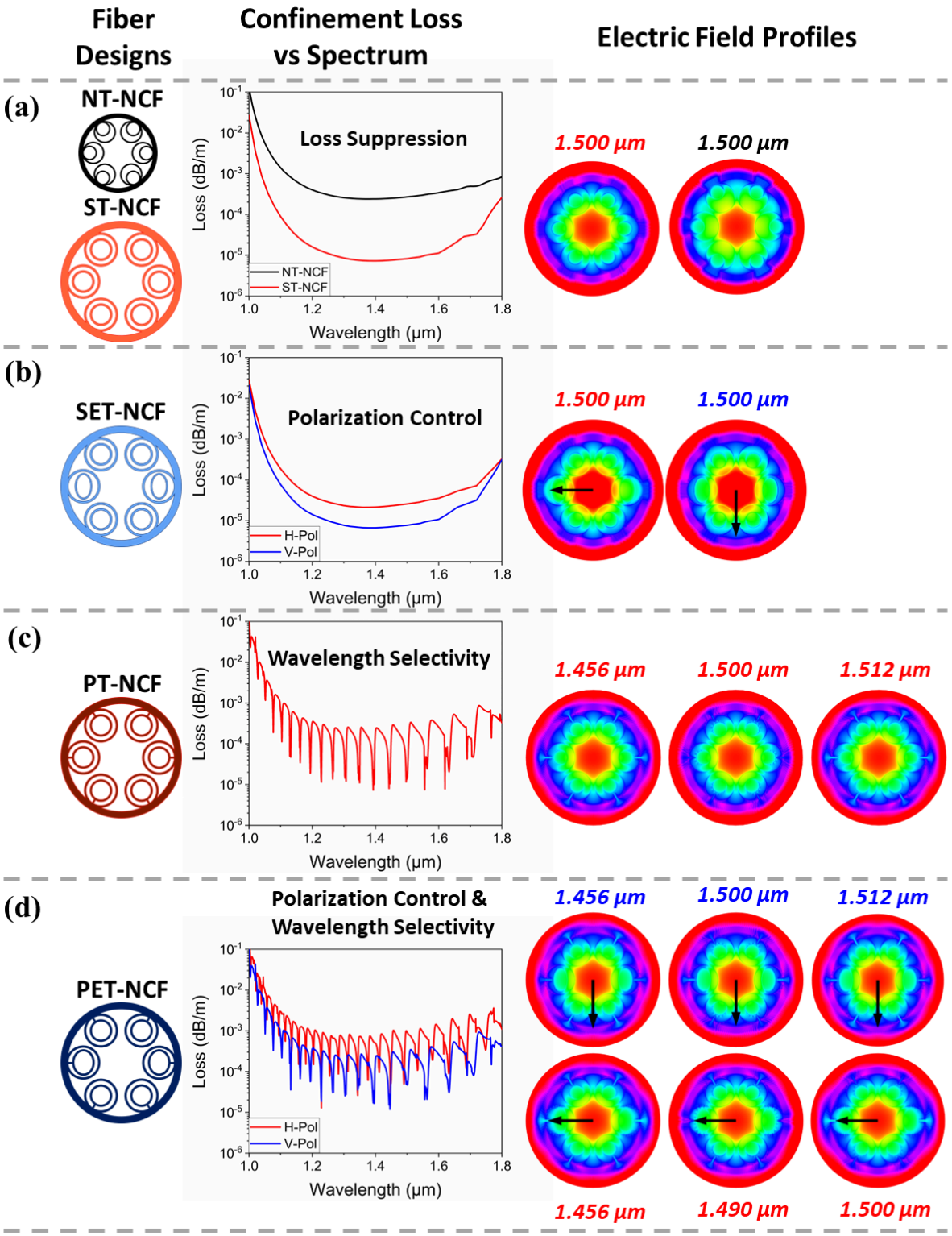


Figure 2

Modal confinement tailoring in NCFs with loss spectrum (center) and representative normalized $|E|^2$ mode profiles at $\lambda = 1.500\ \mu m$. (a) Effect of nested-element positioning on confinement loss reduction, comparing ST-NCF (red) with NT-NCF (black), and mode profiles. (b) Effect of nested element type in SET-NCF consisting of circular nested tubes in the vertical direction and elliptical nested tubes in the horizontal direction with $r_x = 1.7$, yielding confinement loss splitting between H-pol (red) and V-pol (blue), and mode profile (arrows indicate polarization orientation. (c) Effect of pole-anchored nested elements in PT-NCF, demonstrating wavelength filtering with a periodic high/low loss response; representative modes are shown at $\lambda = 1.456, 1.500,$ and $1.512\ \mu m$. (d) Effect of nested element type with pole supports in PET-NCF comprising a pole-anchored elliptical nested tube in horizontal direction with $r_x=1.7$ and pole-anchored round nested tubes in vertical direction, showing spectral filtering with polarization-dependent loss shifts. Mode profiles are shown *at* $\lambda = 1.456, 1.500$, and $1.512\ \mu m$ for V-pol (blue) and $\lambda = 1.456, 1.490,$ and $1.500\ \mu m$ for H-pol (red).

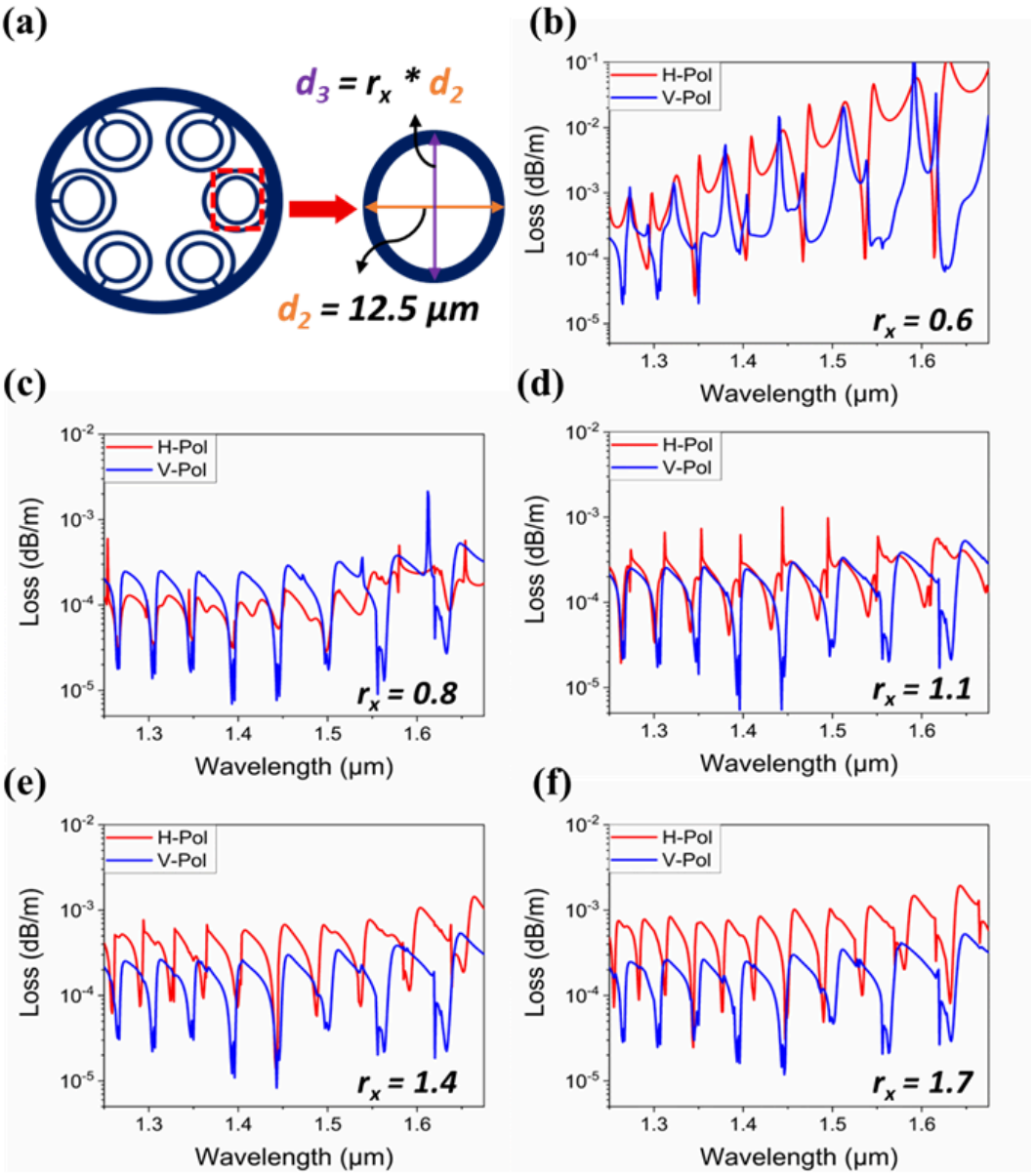


Figure 3

Effect of the ellipticity r_x on the polarization-resolved confinement loss spectra of PET-NCF. (a) Schematic of PET-NCF showing elliptical cladding element in horizontal direction and its ellipticity ratio defined as $r_x = d_3/d_2$ at $d_2 = 12.5\ \mu m$. (b–f) Calculated confinement loss for H-pol (red) and V-pol (blue)

over *1.25–1.675 μm* for r_x = *0.6, 0.8, 1.1, 1.4,* and *1.7*, demonstrating that the spectral minima/maxima and the H/V-pol loss splitting vary systematically with r_x.

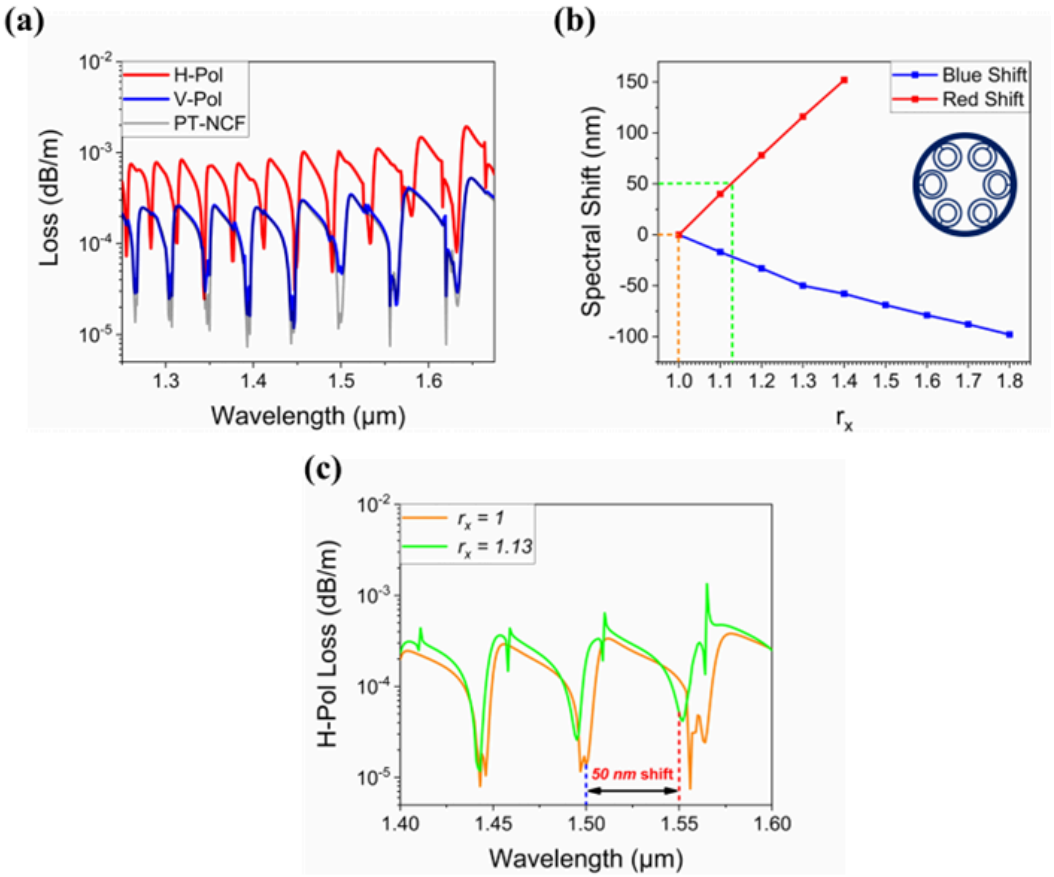


Figure 4

(a) Confinement loss spectra of PET-NCF at r_x= *1.7* with PT-NCF response superimposed for reference. H-pol tuning of the *1.500 μm* filtered wavelength in PET-NCF, (b) spectral shift as a function of the

ellipticity ratio r_x, where red (positive) and blue (negative) shifts correspond to displacement of the filtered wavelength s and (c) an example tuning range of *~50 nm*, shifting the filtered wavelength from *1.50 μm* at r_x= *1.00* to *1.55 μm* at r_x= *1.13*.

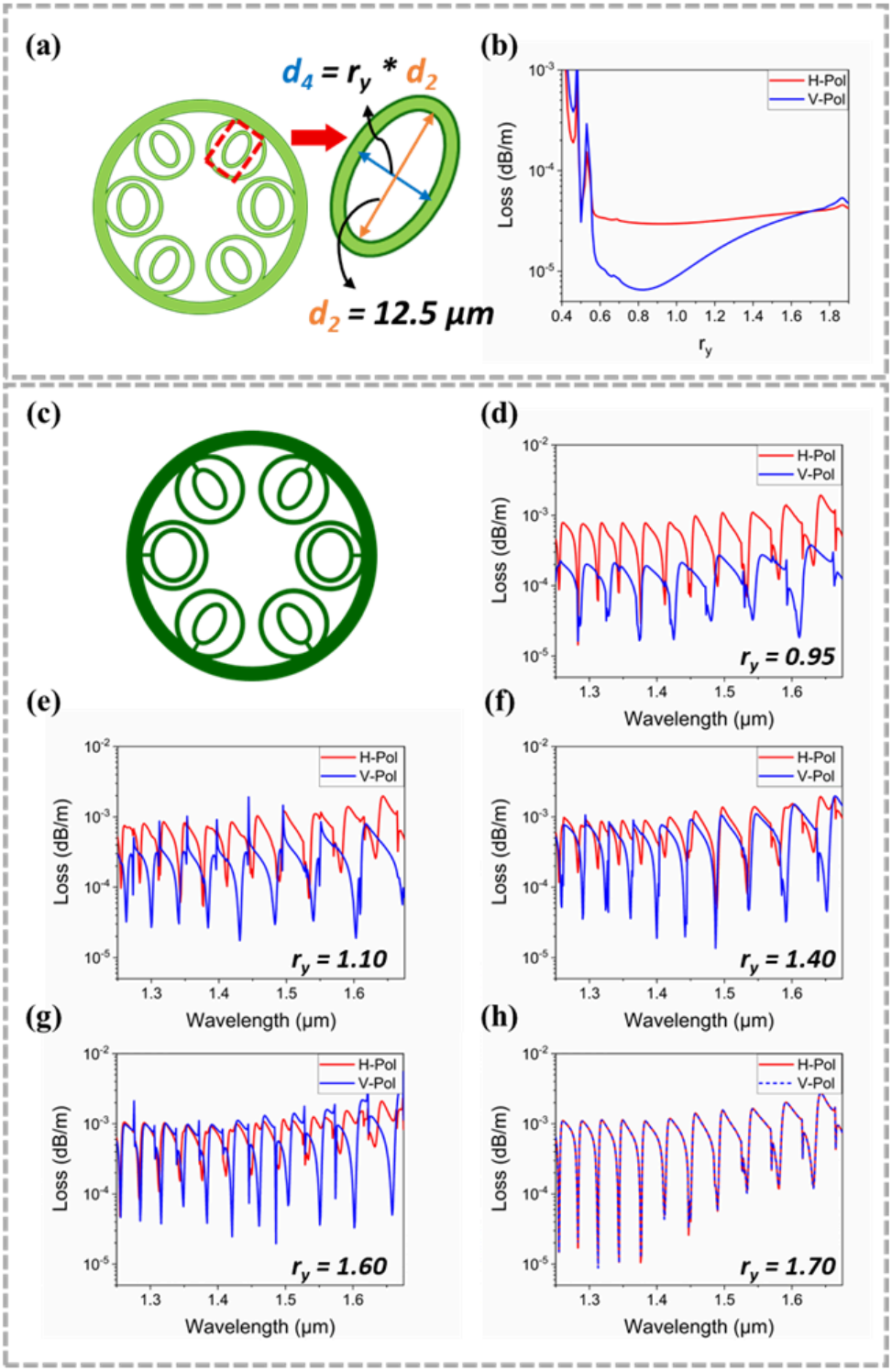
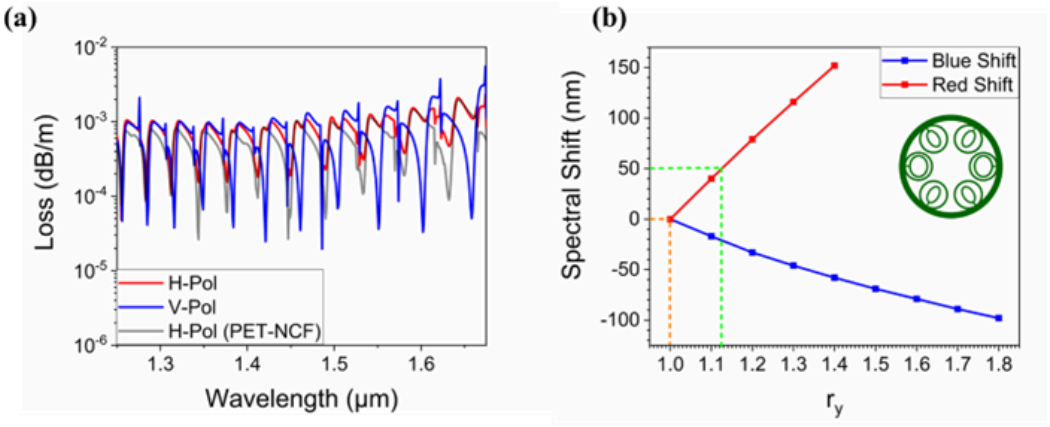


Figure 5

Effect of the ellipticity r_y on the polarization resolved confinement loss spectra of PE-NCF. (a) Schematic of SE-NCF showing elliptical cladding element in vertical direction and its ellipticity ratio defined as $r_y = d_4/d_2$ at $d_2 = 12.5\ \mu m$ and $r_x = 1.7$. (b) Parametric sweep of r_y over *0.4-1.9* at *1.55 μm*. (c) Schematic of PE-NCF with the same ellipticity ratio defined as in SE-NCF. (d-h) Calculated confinement loss for H-pol (red) and V-pol (blue) over *1.250–1.675 μm* for r_y = *0.95, 1.1, 1.4, 1.6,* and *1.7* at $r_x = 1.7$, demonstrating that the spectral minima/maxima and the H/V loss splitting vary systematically with r_y.



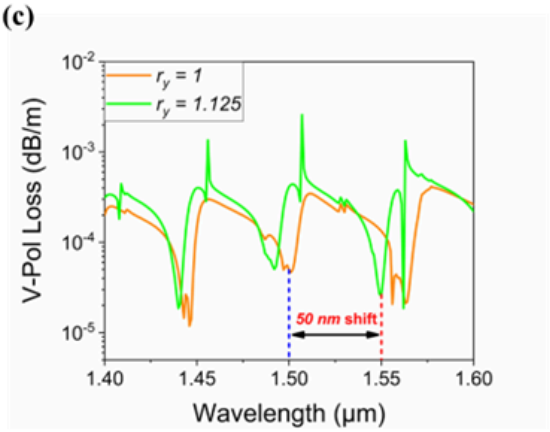


Figure 6

(a) Confinement loss spectra of PE-NCF at $r_y = 1.6$ & $r_x = 1.7$ with PET-NCF H-pol response at $r_x = 1.7$ superimposed for reference. V-pol tuning of the *1.500 μm* filtered wavelength in PE-NCF. (b) Spectral shift as a function of the ellipticity ratio r_y, where red (positive) and blue (negative) shifts correspond to displacement of the filtered wavelength toward longer and smaller wavelengths, respectively, and (c) an example tuning range of *∼50 nm*, shifting the filtered wavelength from *1.500 μm* at $r_y = 1.00$ to *1.550 μm* at $r_y = 1.125$.

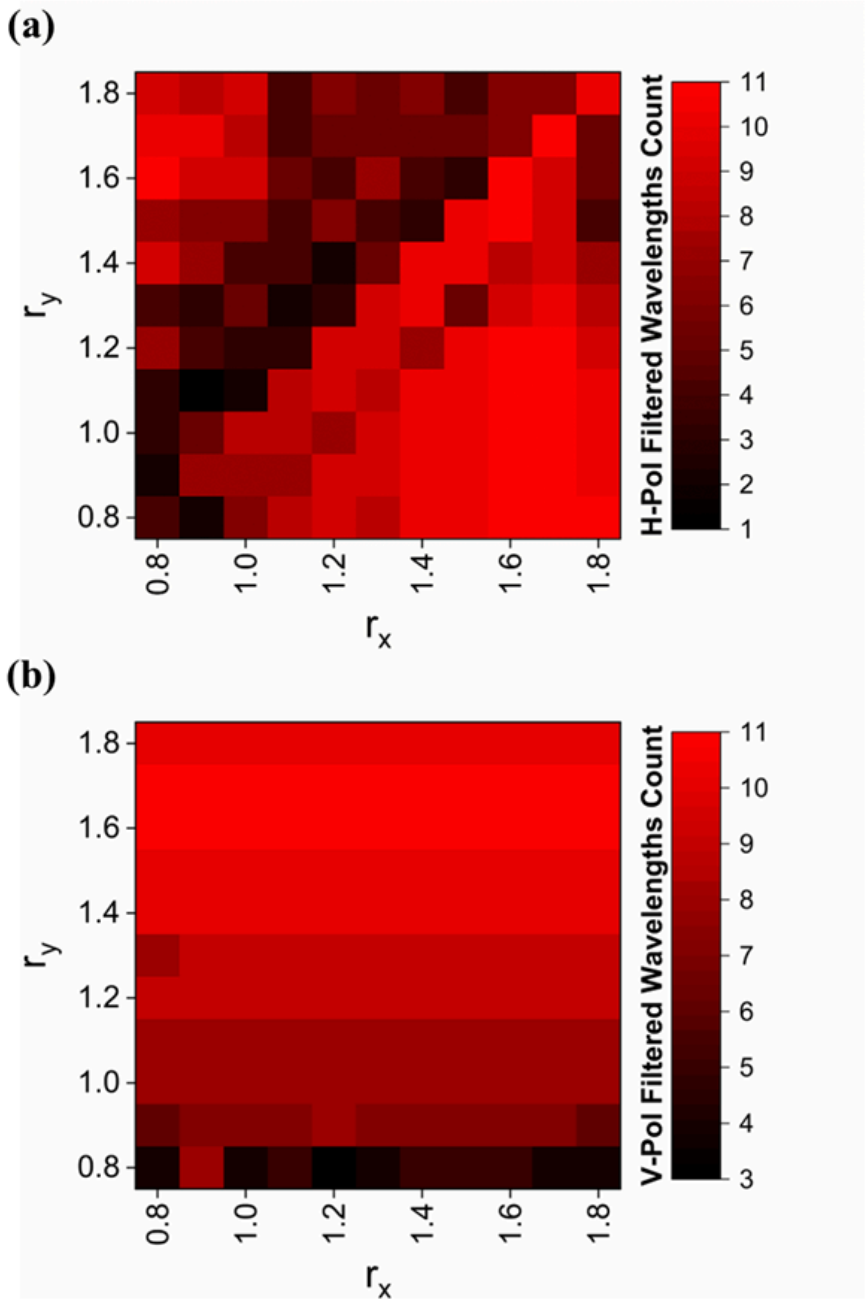


Figure 7

Contour maps of the number of filtered wavelengths within the *1.25 – 1.675 μm* spectral range as a function of the ellipticity ratios r_x and r_y for (a) H-pol and (b) V-pol.